Virtual tissue microstructure reconstruction by deep learning and fluorescence microscopy

Nicolás Bettancourt[1,2,3*], Cristian Pérez[1,2], Valeria Candia[1,2], Pamela Guevara[3], Yannis Kalaidzidis[4], Marino Zerial[4], Fabián Segovia-Miranda[1,2‡], Hernán Morales-Navarrete [5*‡]

1. Department of Cell Biology, Faculty of Biological Sciences, Universidad de Concepción, Concepción, Chile.
2. Grupo de Procesos en Biología del Desarrollo (GDeP), Faculty of Biological Sciences, Universidad de Concepción, Chile.
3. Department of Electrical Engineering, Faculty of Engineering, Universidad de Concepción, Concepción, Chile.
4. Max Planck Institute of Molecular Cell Biology and Genetics, Dresden, Germany.
5. Department of Systems Biology of Development, University of Konstanz, Germany.

* These authors contributed equally to this work.
‡ For correspondence: hernan.morales-navarrete@uni-konstanz.de(HM-N), fabiansegovia@udec.cl (FS-M)

Abstract

Analysis of tissue microstructure is essential for understanding complex biological systems in different species. Studying the three-dimensional (3D) microstructure of tissues, such as the liver, is particularly fascinating due to its essential roles in metabolic processes and detoxification. The liver, composed of diverse cell types like hepatocytes, stellate cells, endothelial cells, and immune cells, exhibits a highly organized structure. Emerging technologies such as 3D microscopy and fluorescence microscopy offer exciting new possibilities for such analysis. Creating digital models that faithfully represent the inherent 3D architecture requires simultaneous imaging of multiple markers across large volumes, hindered by limitations such as poor antibody penetration, restrictions on fluorescent markers, and time-intensive procedures. Here, we present a generic approach for virtual 3D tissue microstructure reconstruction through the integration of Generative Adversarial Networks (GANs) and fluorescence microscopy. We applied our approach for multi-species analysis of tissue microstructure in mouse, frog, and human liver tissue, leveraging the benefits of deep learning and fluorescence microscopy. Our approach can generate accurate and high-resolution predictions of multiple tissue components, such as bile canaliculus, sinusoids and Kupffer cell shapes from images of the actin meshwork in these different species, allowing for efficient and reliable analysis. Moreover, the virtual prediction toolbox is open-source and easily accessible, making it a valuable tool for researchers with a range of expertise levels. We demonstrate the effectiveness of our methods with analysis of tissue microstructure in mouse, frog, and human liver tissue, showcasing its ability to accurately predict differences between species. Overall, our virtual prediction approach provides a powerful and efficient approach to multi-species tissue microstructure analysis.

Introduction

The elucidation of tissue microstructure, encompassing the intricate arrangement and organization of cells, extracellular matrix, and other components within biological tissues, holds paramount significance in biological research(Mayer et al., 2012; Tanaka et al., 2017; Yadid et al., 2022; Yamaguchi et al., 2021). Of particular interest is the exploration of three-dimensional (3D) tissue microstructure, such as that observed in the liver, given its intricate organization and indispensable roles in metabolic, detoxification, and synthesis processes(Hoehme et al., 2010; Segovia-Miranda et al., 2019). The liver, comprising diverse cell types including hepatocytes, stellate cells, endothelial cells, and immune cells, exhibits a remarkably ordered arrangement(Morales-Navarrete et al., 2019a). The spatial distribution and interactions among these cells play a critical role in governing the liver's proper functionality(Baratta et al., 2009; Bouwens et al., 1992). Notably, hepatocytes together with the sinusoidal endothelial cells, form distinct hexagonal patterns, referred to as the liver lobule, which optimizes the exchange of nutrients and bile secretion(Bouwens et al., 1992).

Unraveling the 3D microstructure of the liver and other tissues offers invaluable insights into tissue development, disease progression, and therapeutic responses(Segovia-Miranda et al., 2019). Perturbations in tissue microstructure often manifest during various pathological conditions, including fibrosis, inflammation, and tumor growth(Abdelmalek, 2021). In-depth investigations of such alterations facilitate a deeper comprehension of disease mechanisms and the identification of potential targets for diagnostic and therapeutic interventions(Popa et al., 2021; Ray, 2020). Yet, capturing and reconstructing the 3D tissue microstructure accurately pose considerable challenges with traditional and even advanced methodologies. Reconstructing digital tissue models harboring innate 3D architecture presents a formidable challenge, as it entails the simultaneous imaging of multiple markers, such as antibodies, chimeric proteins, and small fluorescent molecules, across extensive volumes. The limitations of this endeavor encompass obstacles like inadequate antibody penetration, restrictions on the number of concurrently imaged fluorescent markers, and considerable acquisition time encompassing sample preparation and imaging procedures. Addressing these bottlenecks holds the key to advancing the field of 3D tissue modeling.

Over the past decade, deep learning has emerged as a groundbreaking technique in machine learning, showcasing its remarkable ability to unravel intricate patterns and representations from vast and complex datasets(LeCun et al., 2015). Deep learning has revolutionized the realm of artificial intelligence by eliminating the need for manual feature engineering. It employs artificial neural networks, inspired by the intricate connectivity of biological neural networks in the human brain, to automatically learn and discern intricate features directly from the data(Hallou et al., 2021; LeCun et al., 2015). By leveraging multiple layers of interconnected nodes, deep neural networks harness their hierarchical structure to progressively extract increasingly abstract and meaningful representations of the input data(Aloysius and Geetha, 2017). This learning technique has achieved unprecedented successes in critical tasks such as image classification, object detection, and image segmentation. A distinctive area where deep learning's prowess shines prominently is in the field of biology, particularly the analysis of microscopy images(Hallou et al., 2021; McQuin et al., 2018; Moen et al., 2019). Microscopy, an indispensable tool in biological research, enables the study of cellular and subcellular structures, unraveling the intricate workings of life. Deep learning models applied to microscopy image analysis have showcased their capability to

automatically segment and classify cells, track their dynamic movements, and extract intricate features(Christiansen et al., 2018; Hallou et al., 2021; McQuin et al., 2018; Moen et al., 2019; Naert et al., 2021; Ounkomol et al., 2018; Xing et al., 2018). This transformative technology empowers researchers to investigate cellular dynamics, identify disease biomarkers, and expedite the discovery of novel therapeutics.

Previously, we used convolutional neural networks (CNN) to predict tissue structures by learning features embedded within single-marker images(Morales-Navarrete et al., 2019b). In particular, our deep learning framework showed a remarkable accuracy for the prediction of the bile canaliculi (BC) and sinusoidal networks from images of the actin meshwork of liver tissue. However, this approach has several limitations: i) requiring a pair of images of the BC/Sinusoids and the actin mesh, which is not always technically possible, ii) using a 2D approach to predict 3D structures can cause loss of data information, iii) is limited to healthy mouse liver tissue. Here, we propose an approach for virtual tissue microstructure reconstruction through the integration of Generative Adversarial Networks (GANs)(Goodfellow et al., n.d.) and fluorescence microscopy. By harnessing the strengths of GANs and leveraging the high-resolution imaging capabilities offered by fluorescence microscopy, we aim to surmount the limitations encountered by previous methods. Our primary objective is to deliver a more detailed and accurate representation of the 3D tissue microstructure, focusing specifically on the liver in different species such as mouse, frog and human. This pioneering approach holds immense potential for enabling a deeper understanding of tissue microstructure in both healthy and diseased states.

Results

CNNs accurately predict several tissue structures in mouse liver tissue

We utilized a convolutional neural network (CNN) to accurately predict various components of liver tissue microstructure based on high-resolution images of the actin mesh. These images were acquired using confocal microscopy, enabling us to capture detailed and precise representations of the different components present in liver tissue. To accomplish our predictions, we employed two distinct network architectures in 2D and 3D: a modified version of UNet(Ronneberger et al., 2015) and CycleGAN(Zhu et al., 2017). The modified UNet architecture, depicted in Figure 1-a (refer to the Methods section for comprehensive details), was trained using a dataset consisting of spatially registered pairs of 3D images. The cortical actin mesh served as the input image, while the output images included the BC network, sinusoids, and Kupffer cells. In contrast, for the CycleGAN approach, we employed computational mixing of the image pair to simulate unpaired images, thereby avoiding the requirement for paired images.

The qualitative assessment of our predictions, visually compared to the ground truth images presented in Figure 1-b, revealed highly promising results for all the approaches we employed. Both the UNet and CycleGAN architectures generated outputs that closely resembled the ground truth images, indicating their effectiveness in accurately predicting the different components of liver tissue microstructure from the actin mesh images. To ensure a comprehensive evaluation of our predictions, we conducted extensive tests specifically

targeting the accuracy of predicting the BC component. Surprisingly, our results showed no substantial differences between the 2D and 3D architectures, as depicted in Supplementary Figure 1. However, the computational costs for training 3D CNNs are much higher than the ones needed for 2D architectures. It is noteworthy that the majority of errors were primarily concentrated near the veins, where the antibody stainings exhibited lower specificity, as illustrated in Supplementary Figure 2.

For a rigorous quantitative assessment, we employed various evaluation metrics, including Mean Squared Error, Mean Squared Logarithmic Error, Mean Absolute Error, Root Mean Squared Error, Peak Signal-to-Noise Ratio, Structural Similarity Index Measure, Multi-scale Structural Similarity Index Measure, Cosine Similarity, and Coefficient of Correlation. These metrics enabled us to thoroughly analyze the performance of our predictions, both in the context of the entire images and by separately considering the background and foreground regions. Detailed information regarding these evaluations can be found in the Methods section and Supplementary Figure 1. Remarkably, both the UNet and CycleGAN architectures consistently exhibited similar performance across all evaluated structures, as demonstrated in Figure 1-c and Supplementary Figure 1. This indicates that both approaches are equally effective in predicting the components of liver tissue microstructure. However, it is worth mentioning that the major advantage of the CycleGAN approach is its ability to generate accurate predictions without relying on paired images. This characteristic enhances its flexibility and practical applicability in various scenarios.

CycleGAN accurately predicts BC and sinusoidal networks for deep tissue reconstruction

Given the generality and high performance demonstrated by CycleGAN in our initial experiments, we proceeded to test its capabilities in more challenging tasks. In particular, we aimed to investigate whether CycleGAN could effectively predict the intricate structures of the BC and sinusoidal networks in the context of deep tissue imaging. Traditional 3D imaging methods face inherent limitations when it comes to imaging deep tissue regions beyond a depth of approximately 80 to 100 micrometers, especially when utilizing antibody markers for specific structures such as the BC and sinusoids. The limited penetrance of antibodies within the tissue hampers the visualization of these structures beyond the shallow surface layers.

However, we capitalized on the unique properties of small fluorescent molecules, such as Phalloidin, which specifically stains the actin mesh. Phalloidin has the remarkable ability to penetrate several hundred microns into the tissue, surpassing the constraints of antibody staining. Leveraging this advantage, we acquired high-resolution images of the actin mesh at a depth of 300 microns, well beyond the typical imaging range achievable with antibody-based techniques. Using our pre-trained CycleGAN models, we then embarked on the task of predicting both the BC and sinusoidal structures from these deep tissue images. Surprisingly, our approach yielded accurate predictions of these structures throughout the entire depth of the images, exceeding the limitations imposed by the restricted antibody staining penetration depth of 80 microns. This is visually depicted in Figure 2a and Supplementary Figure 3.

The successful application of CycleGAN in predicting structures beyond the experimentally accessible depth of antibody staining represents a major advancement in the field of deep tissue imaging. Our approach not only obviates the need for laborious and time-consuming

antibody-based techniques but also offers a significant reduction in imaging costs. Moreover, by enabling the reconstruction of tissue structures that were previously inaccessible using conventional methods, our approach opens new avenues for exploring the intricate details of deep tissue microarchitecture.

The ability to obtain deep tissue reconstructions using a readily available marker, such as Phalloidin, streamlines experimental procedures and expedites data acquisition. Furthermore, the successful prediction of structures beyond the limitations of antibody staining holds great potential for numerous research fields and clinical applications, revolutionizing our understanding of deep tissue biology and paving the way for groundbreaking discoveries.

Accurate prediction of tissue microstructure in human liver tissue

To further push the boundaries of our approach, we sought to tackle an even more challenging task: predicting the bile canaliculi (BC) structures in human liver tissue. Overcoming this challenge required addressing the practical limitation of not being able to obtain paired images of the actin mesh and BC simultaneously in human tissue samples. Given the experimental constraints outlined in Segovia-Miranda et al. (2019)(Segovia-Miranda et al., 2019), where simultaneous imaging of the actin mesh and BC in human tissue samples was deemed infeasible, we devised a strategy to train our CycleGAN using independent sets of images representing the actin mesh and BC from different samples and patients Figure 2b-middle.

Our trained CycleGAN network exhibited a remarkable ability to generate visually convincing predictions of the BC in human liver tissue, as demonstrated in Figure 2b-middle. Additionally, we tested if the network trained in mouse tissue samples could predict BC structures in human tissue. Surprisingly, the network was able to produce highly accurate predictions despite being originally trained on mouse data (Figure 2b, bottom). The fact that the network trained on mouse data could successfully generalize its predictions to human tissue underscores the remarkable conservation of BC structures across species. These findings provide valuable insights into the structural similarities and functional significance of BC in both mouse and human liver biology. The successful application of our CycleGAN approach in predicting BC structures in the absence of paired images highlights the adaptability and robustness of our method. Moreover, it suggests that the underlying architecture and organization of BC are highly conserved across different species.

Discussion

The analysis of tissue microstructure is a critical task in various fields of research, but current methods often suffer from limitations, require significant expertise, and can be time-consuming. Creating digital models of tissue microstructure typically involves simultaneous imaging of multiple markers across large volumes. However, this process is hindered by various limitations, including poor antibody penetration, restrictions on fluorescent markers, and the need for time-intensive procedures. Deep learning models applied to microscopy image analysis have emerged as a promising solution for predicting tissue structures. Our study demonstrates the successful application of CycleGAN in predicting structures beyond the experimentally accessible depth of antibody staining, representing a significant advancement in the field of deep tissue imaging. By leveraging the power of deep learning, we have surpassed the limitations of traditional methods and achieved accurate predictions of tissue microstructure.

The utilization of a simple marker, such as Phalloidin, in our method further enhances its practicality and broadens its applicability. Unlike the complex and time-consuming procedures required for simultaneous imaging of multiple markers, our approach relies on a single marker, making it more efficient and cost-effective. This simplicity enables researchers to obtain deep tissue reconstructions with ease, providing a valuable tool for investigating tissue microstructure. Moreover, our method can even be applied in the absence of specific markers, as it only requires a few manually annotated structures. This flexibility allows researchers to utilize our approach in situations where specific markers may not be available or suitable. For instance, in Figure 2c, we showcased the successful prediction of bile canaliculi (BC) in xenopus liver tissue, where antibodies for BC were not available. The network was trained using only one annotated image and generated visually impressive results. However, it is important to acknowledge that this approach has limitations and may produce some artifacts. A larger training set with more annotated images could potentially improve the results and reduce such artifacts.

The ability to predict BC structures in human liver tissue using our CycleGAN approach, despite the inherent challenges and limitations, represents a significant breakthrough. This achievement not only expands our understanding of liver tissue microarchitecture in the context of human biology but also opens up new avenues for investigating the role of BC in various liver diseases and clinical applications. Our results demonstrate the power of leveraging computational methods and deep learning techniques to overcome experimental constraints and provide valuable insights into complex biological systems. The successful translation of our approach from mouse to human liver tissue holds great promise for advancing our understanding of liver biology and facilitating the development of novel diagnostic and therapeutic strategies for liver-related disorders.

Our study presents a novel approach for analyzing tissue microstructure using deep learning models and demonstrates its effectiveness in predicting structures beyond the limitations of conventional methods. The simplicity and versatility of our method, particularly with the use of a single marker or minimal annotations, make it a valuable tool for research in various systems. Future improvements, such as expanding the training dataset and refining the network architecture, have the potential to further enhance the accuracy and reliability of our

predictions, ultimately advancing our understanding of tissue microarchitecture and its implications in biological systems.

Methods

Animals

Adult C57BL/6J mice (8-10 weeks old) were obtained from the animal facility (Centro Regional de Estudios Avanzados para la Vida (CREAV)) at the Universidad de Concepción. The animals were maintained in strict pathogen-free conditions and received *ad libitum* feeding. All procedures performed were approved by the vice rectory of ethics and biosecurity committee from the investigation and development of Universidad de Concepción. Z-stack images of NAFLD human liver samples were obtained from(Segovia-Miranda et al., 2019). Fixed Xenopus liver were donated by Sylvain Marcellini (Universidad de Concepción)

Mice and Xenopus liver collection and immunostaining

Mice livers were fixed through intracardiac perfusion with 4% paraformaldehyde 0.1% Tween-20/PBS and post-fixed overnight with the same solution at room temperature. Xenopus livers were fixed by immersion in 4% paraformaldehyde 0.1% Tween-20/PBS for 4 days at room temperature. 100 µm thick liver sections were obtained with a vibratome. Immunolabeling and optical clearing were performed as described previously(Morales-Navarrete et al., 2019a).

Imaging

Liver samples were imaged (0.3 µm voxel size) in an inverted multiphoton laser-scanning microscope (Zeiss LSM 780) using a 40x1.2 numerical aperture multi-Immersion objective (Zeiss). DAPI was excited at 780 nm using a Chameleon Ti-Sapphire 2-photon laser. Alexa Fluor 488, 555 and 647 were excited with 488, 561 and 633 laser lines and detected with Gallium arsenide phosphide (GaAsp) detectors.

Image pre-processing

The different components of liver tissues (BC, sinusoids and cortical mesh) were imaged with high-resolution (voxel size 0.3 x 0.3 x 0.3 µm) fluorescent image stacks (80/100µm depth). To cover the entire CV-PV axes, 2x1 tiles were stitched using the image stitching plug-in of Fiji(Preibisch et al., 2009). The 3D images were first denoised using the PURE-LET algorithm(Luisier et al., 2010) with the maximum number of cycles. Then, a background and shading correction was performed using the tool BaSiC(Peng et al., 2017) along the stack. Finally, all channels were aligned to the actin mesh channels using the function Correct 3D Drift from Fiji.

Cycle-GAN network Architecture

The model consists of two Generators and two Discriminators. Generator A to B (G-AB) takes an image (real) of class A as input and generates an image (fake) of class B as output. On the other hand, Generator B to A (G-BA) takes an image (real) of class B as input and generates an image (fake) of class A as output. Discriminator A (D-A) classifies images generated by G-BA as reap or fake, whilst Discriminator B (D-B) classifies images generated by G-AB as real or fake. The objective is to train both generators and both discriminators. This process will, eventually, allow the generators to create realistic enough fake images and deceive the discriminators.

Generator architecture: The architecture for models trained with patches of size 128x128 pixels: c7s1-64, d128, d256, R256 (x6), u128, u64, c7s1-1. The architecture for models trained with patches of size 256x256 pixels: c7s1-64, d128, d256, R256 (x9), u128, u64, c7s1-1. Where: c7s1-k is a convolution of k filters of size 7x7 and stride 1, followed by an Instance

Normalization (IN) layer and a ReLU layer, dk is a convolution of k filters of size 3x3 with stride 2, followed by an IN layer and a ReLU layer, Rk is a residual block with two convolutions with equal number of filters of size 3x3, uk is a block of a transposed convolution with k filters of size 3x3 and stride 2, followed by an IN layer and a ReLU layer. Discriminator architecture: The architecture for both discriminators is: C64 - C128 - C256 - C512 - F1. Where: Ck is a block of a convolution of k filters of size 4x4, followed by an IN layer and a LeakyReLU layer, F1 is a convolution of 1 filter of size 4x4.

The network for the 3D model is essentially the same as the 2D model, with minor differences only: the 2D input and output layers were adapted to accept and produce 3D patches, respectively, and all 2D convolution layers were swapped for 3D convolution layers.

Model Training

CycleGAN 2D: Four images, two for each domain, were used to train the 2D models. Pixel values were normalized between -1 and 1. 2500 two-dimensional patches were extracted from each image, leading to 5000 patches per domain. Patches of size 128x128 pixels were used for the membrane/BC and the membrane/sinusoids models, whereas patches of size 256x256 pixels were used for the membrane/Kupffer model. All models were trained for 100 epochs using Adam optimizer with a learning-rate of 0.002, a beta value of 0.5, a batch-size of 1 and Mean Squared Error as the loss function.

CycleGAN 3D: Four images, two for each domain, were used to train the 3D model. Pixel values were normalized between -1 and 1. For the membrane/BC model, 900 three-dimensional patches of size 64x64x64 pixels were extracted from each image, leading to 1800 patches per domain. The ninety percent of the patches were used for training and the remaining ten percent were used for validation. Hyperparameters for the 3D model were set to be equal to those of the 2D model, except for the number of epochs which was set to 300. This allowed us to stop the training early if no improvements were observed.

Author Contributions

H.M-N. conceived the project. H.M-N and F.S-M designed and supervised the project. H.M-N, F.S-M, P.G., Y.K and M.Z. developed the conceptual bases of the project. V.C., C.P., and F.S-M. performed the immunofluorescence, optical clearing, and imaging. N.B and H.M-N. implemented the deep convolutional neural networks and analysis pipelines. N.B., and H.M-N. performed the data analysis and interpretation of the results. F.S-M. and H.M-N. wrote the manuscript.

Financial support and sponsorship

This work was financially supported by Fondecyt (grant # 1200965).

Conflict of interest

Authors declare no conflict of interest.

Keywords

3D geometrical models, optical clearing, convolutional neural networks, deep learning

Acknowledgments

We are grateful to Sylvain Marcellini (Universidad de Concepción) for the Xenopus liver samples. We would like to thank the following Facilities from Universidad de Concepción for their support: Centro de Microscopía Avanzada (CMA BIO-BIO) and Centro Regional de Estudios por la Vida (CREAV).

References

Abdelmalek MF. 2021. Nonalcoholic fatty liver disease: another leap forward. *Nat Rev Gastroentero* **18**:85–86. doi:10.1038/s41575-020-00406-0

Aloysius N, Geetha M. 2017. A review on deep convolutional neural networks. *2017 Int Conf Commun Signal Process ICCSP* 0588–0592. doi:10.1109/iccsp.2017.8286426

Baratta JL, Ngo A, Lopez B, Kasabwalla N, Longmuir KJ, Robertson RT. 2009. Cellular organization of normal mouse liver: a histological, quantitative immunocytochemical, and fine structural analysis. *Histochemistry and Cell Biology* **131**:713–726. doi:10.1007/s00418-009-0577-1

Bouwens L, Bleser PD, Vanderkerken K, Geerts B, Wisse E. 1992. Liver Cell Heterogeneity: Functions of Non-Parenchymal Cells. *Enzyme* **46**:155–168. doi:10.1159/000468782

Christiansen EM, Yang SJ, Ando DM, Javaherian A, Skibinski G, Lipnick S, Mount E, O'Neil A, Shah K, Lee AK, Goyal P, Fedus W, Poplin R, Esteva A, Berndl M, Rubin LL, Nelson P, Finkbeiner S. 2018. In Silico Labeling: Predicting Fluorescent Labels in Unlabeled Images. *Cell* **173**:792-803.e19. doi:10.1016/j.cell.2018.03.040

Goodfellow I, Pouget-Abadie J, Mirza M, Xu B, Warde-Farley D, Ozair S, Courville A, Bengio Y. n.d. Generative Adversarial NetsAdvances in Neural Information Processing Systems. Curran Associates, Inc.

Hallou A, Yevick HG, Dumitrascu B, Uhlmann V. 2021. Deep learning for bioimage analysis in developmental biology. *Dev Camb Engl* **148**:dev199616. doi:10.1242/dev.199616

Hoehme S, Brulport M, Bauer A, Bedawy E, Schormann W, Hermes M, Puppe V, Gebhardt R, Zellmer S, Schwarz M, Bockamp E, Timmel T, Hengstler JG, Drasdo D. 2010. Prediction and validation of cell alignment along microvessels as order principle to restore tissue architecture in liver regeneration. *Proceedings of the National Academy of Sciences* **107**:10371–10376. doi:10.1073/pnas.0909374107

LeCun Y, Bengio Y, Hinton G. 2015. Deep learning. *Nature* **521**:436–44. doi:10.1038/nature14539

Luisier F, Vonesch C, Blu T, Unser M. 2010. Fast interscale wavelet denoising of Poisson-corrupted images. *Signal Process* **90**:415–427. doi:10.1016/j.sigpro.2009.07.009

Mayer J, Swoger J, Ozga AJ, Stein JV, Sharpe J. 2012. Quantitative Measurements in 3-Dimensional Datasets of Mouse Lymph Nodes Resolve Organ-Wide Functional Dependencies. *Comput Math Methods Medicine* **2012**:128431. doi:10.1155/2012/128431

McQuin C, Goodman A, Chernyshev V, Kamentsky L, Cimini BA, Karhohs KW, Doan M, Ding L, Rafelski SM, Thirstrup D, Wiegraebe W, Singh S, Becker T, Caicedo JC, Carpenter AE. 2018. CellProfiler 3.0: Next-generation image processing for biology. *PLOS Biology* **16**:e2005970. doi:10.1371/journal.pbio.2005970

Moen E, Bannon D, Kudo T, Graf W, Covert M, Valen DV. 2019. Deep learning for cellular image analysis. *Nat Methods* **16**:1233–1246. doi:10.1038/s41592-019-0403-1

Morales-Navarrete H, Nonaka H, Scholich A, Segovia-Miranda F, Back W de, Meyer K, Bogorad RL, Koteliansky V, Brusch L, Kalaidzidis Y, Jülicher F, Friedrich BM, Zerial M. 2019a. Liquid-crystal organization of liver tissue. *Elife* **8**:e44860. doi:10.7554/elife.44860

Morales-Navarrete H, Segovia-Miranda F, Zerial M, Kalaidzidis Y. 2019b. Prediction of Multiple 3D Tissue Structures Based on Single-Marker Images Using Convolutional Neural Networks. *2019 Ieee Int Conf Image Process Icip* **00**:1361–1365. doi:10.1109/icip.2019.8803057

Naert T, Çiçek Ö, Ogar P, Bürgi M, Shaidani N-I, Kaminski MM, Xu Y, Grand K, Vujanovic M, Prata D, Hildebrandt F, Brox T, Ronneberger O, Voigt FF, Helmchen F, Loffing J, Horb

ME, Willsey HR, Lienkamp SS. 2021. Deep learning is widely applicable to phenotyping embryonic development and disease. *Development* **148**:dev199664. doi:10.1242/dev.199664

Ounkomol C, Seshamani S, Maleckar MM, Collman F, Johnson GR. 2018. Label-free prediction of three-dimensional fluorescence images from transmitted light microscopy. *Nat Methods* **15**:917–920. doi:10.1038/s41592-018-0111-2

Peng T, Thorn K, Schroeder T, Wang L, Theis FJ, Marr C, Navab N. 2017. A BaSiC tool for background and shading correction of optical microscopy images. *Nat Commun* **8**:14836. doi:10.1038/ncomms14836

Popa SL, Ismaiel A, Cristina P, Cristina M, Chiarioni G, David L, Dumitrascu DL. 2021. Non-Alcoholic Fatty Liver Disease: Implementing Complete Automated Diagnosis and Staging. A Systematic Review. *Diagnostics* **11**:1078. doi:10.3390/diagnostics11061078

Preibisch S, Saalfeld S, Tomancak P. 2009. Globally optimal stitching of tiled 3D microscopic image acquisitions. *Bioinformatics* **25**:1463–1465. doi:10.1093/bioinformatics/btp184

Ray K. 2020. High-definition medicine: modelling NAFLD in 3D. *Nat Rev Gastroenterol Hepatol* **17**:66–67. doi:10.1038/s41575-019-0256-1

Ronneberger O, Fischer P, Brox T. 2015. U-Net: Convolutional Networks for Biomedical Image Segmentation. *arXiv*. doi:10.48550/arxiv.1505.04597

Segovia-Miranda F, Morales-Navarrete H, Kücken M, Moser V, Seifert S, Repnik U, Rost F, Brosch M, Hendricks A, Hinz S, Röcken C, Lütjohann D, Kalaidzidis Y, Schafmayer C, Brusch L, Hampe J, Zerial M. 2019. Three-dimensional spatially resolved geometrical and functional models of human liver tissue reveal new aspects of NAFLD progression. *Nat Med* **25**:1885–1893. doi:10.1038/s41591-019-0660-7

Tanaka N, Kanatani S, Tomer R, Sahlgren C, Kronqvist P, Kaczynska D, Louhivuori L, Kis L, Lindh C, Mitura P, Stepulak A, Corvigno S, Hartman J, Micke P, Mezheyeuski A, Strell C, Carlson JW, Moro CF, Dahlstrand H, Östman A, Matsumoto K, Wiklund P, Oya M, Miyakawa A, Deisseroth K, Uhlén P. 2017. Whole-tissue biopsy phenotyping of three-dimensional tumours reveals patterns of cancer heterogeneity. *Nat Biomed Eng* **1**:796–806. doi:10.1038/s41551-017-0139-0

Xing F, Xie Y, Su H, Liu F, Yang L. 2018. Deep Learning in Microscopy Image Analysis: A Survey. *Ieee T Neur Net Lear* **29**:4550–4568. doi:10.1109/tnnls.2017.2766168

Yadid M, Oved H, Silberman E, Dvir T. 2022. Bioengineering approaches to treat the failing heart: from cell biology to 3D printing. *Nat Rev Cardiol* **19**:83–99. doi:10.1038/s41569-021-00603-7

Yamaguchi M, Yoshihara K, Yachida N, Suda K, Tamura R, Ishiguro T, Enomoto T. 2021. The New Era of Three-Dimensional Histoarchitecture of the Human Endometrium. *J Pers Medicine* **11**:713. doi:10.3390/jpm11080713

Zhu J-Y, Park T, Isola P, Efros AA. 2017. Unpaired Image-to-Image Translation using Cycle-Consistent Adversarial Networks. *arXiv*. doi:10.48550/arxiv.1703.10593

Figures

A

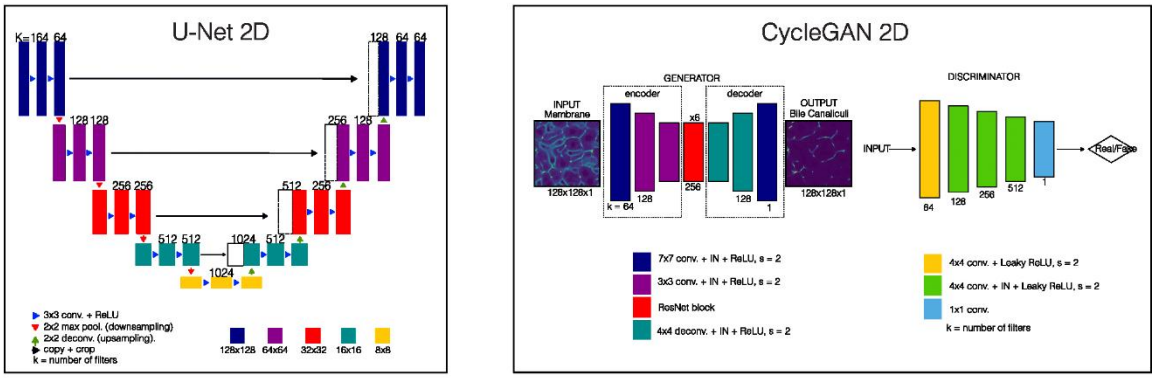
U-Net 2D
K=164 64
128 128
256 256
512 512
1024
128 64 64
256 128
512 256
512 512 1024
3x3 conv. + ReLU
2x2 max pool. (downsampling)
2x2 deconv. (upsampling).
copy + crop
k = number of filters
128x128 64x64 32x32 16x16 8x8
CycleGAN 2D
GENERATOR
INPUT Membrane
encoder
decoder
x6
OUTPUT Bile Canaliculi
128x128x1
k = 64
128
256
128
1
DISCRIMINATOR
INPUT
Real/Fake
64 128 256 512 1
7x7 conv. + IN + ReLU, s = 2
3x3 conv. + IN + ReLU, s = 2
ResNet block
4x4 deconv. + IN + ReLU, s = 2
4x4 conv. + Leaky ReLU, s = 2
4x4 conv. + IN + Leaky ReLU, s = 2
1x1 conv.
k = number of filters

B

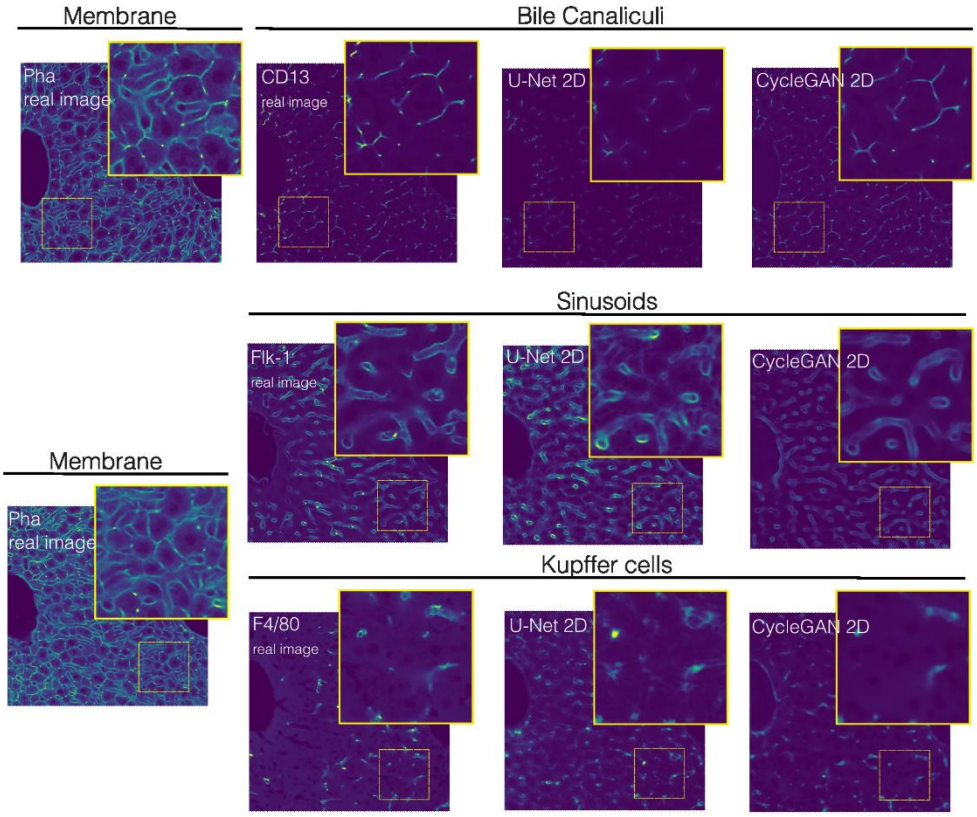
Membrane
Pha
real image
Bile Canaliculi
CD13
real image
U-Net 2D
CycleGAN 2D
Sinusoids
Flk-1
real image
U-Net 2D
CycleGAN 2D
Membrane
Pha
real image
Kupffer cells
F4/80
real image
U-Net 2D
CycleGAN 2D

C

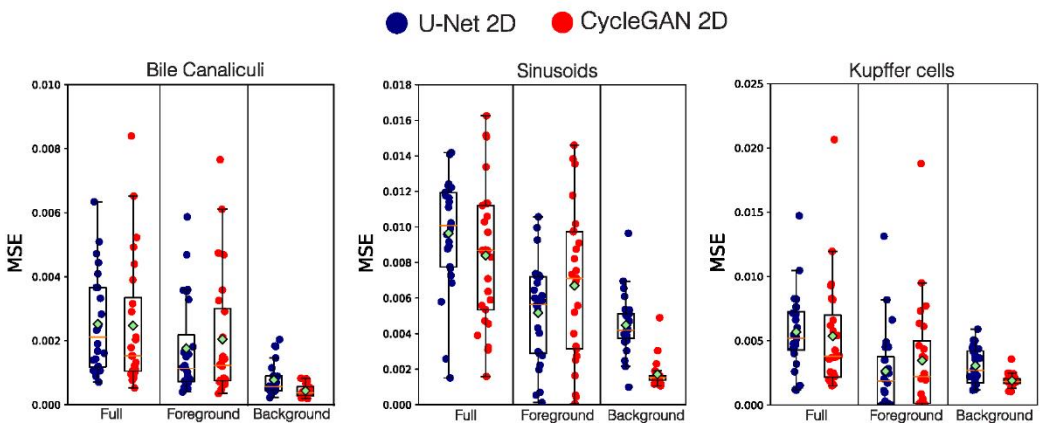
U-Net 2D
CycleGAN 2D
Bile Canaliculi
Sinusoids
Kupffer cells
MSE
Full
Foreground
Background

Fig. 1: Deep convolutional networks accurately predict liver tissue structures from actin mesh images (i.e. membrane images).

(a) Schematic representation of the network architectures used: UNet and CycleGAN. (b) 2D sections of 3D fluorescent images of the actin mesh (membranes), Bile Canaliculi, Sinusoids and Kupffer cells (experimental images) as well as the corresponding predictions by Unet and CycleGAN in 2D. C) Quantification of the performance of the predictions of the BC network generated by the models

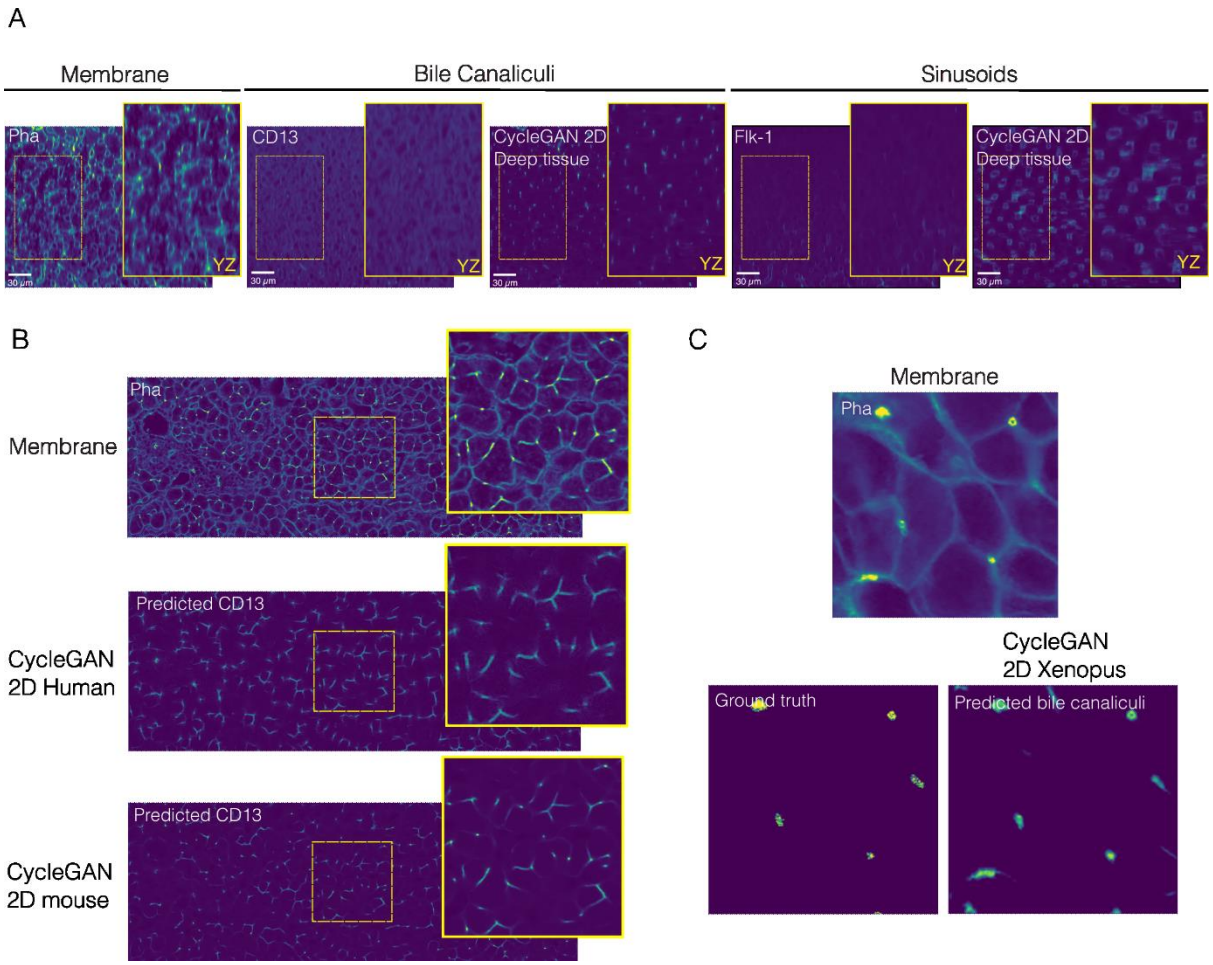

Fig. 2: Applications of CycleGAN for tissue microstructure predictions.
(a) 2D axial sections of 3D fluorescent images of the actin mesh (membranes), Bile Canaliculi, Sinusoids (experimental images) as well as the predictions of the CyCleGAn model, (b) 2D sections of 3D fluorescent images of the actin mesh (membranes) and Bile Canaliculi (experimental images) of human liver tissue together with the corresponding predictions of the CyCleGAN 2D model trained in mouse and human tissue images. c) 2D axial sections of 3D fluorescent images of the actin mesh (membranes), and manually segmented Bile Canaliculi (GT) and the predictions of the CyCleGAN 2D model.

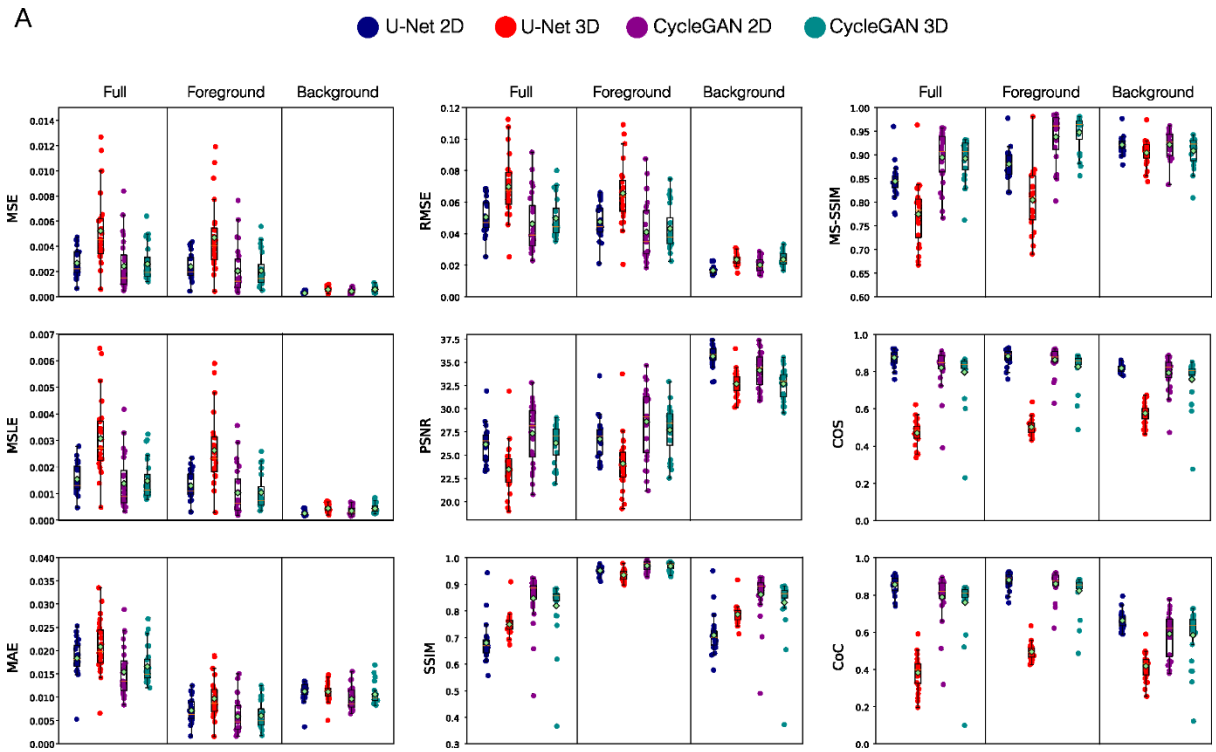

Supp Fig. 1: Quantification of the performance of the predictions.

Quantification of the performance of the predictions of the BC network generated by the 2D and 3D, UNet and CycleGAN models using the following metrics Mean Squared Error, Mean Squared Logarithmic Error, Mean Absolute Error, Root Mean Squared Error, Peak Signal-to-Noise Ratio, Structural Similarity Index Measure, Multi-scale Structural Similarity Index Measure, Cosine Similarity, and Coefficient of Correlation.

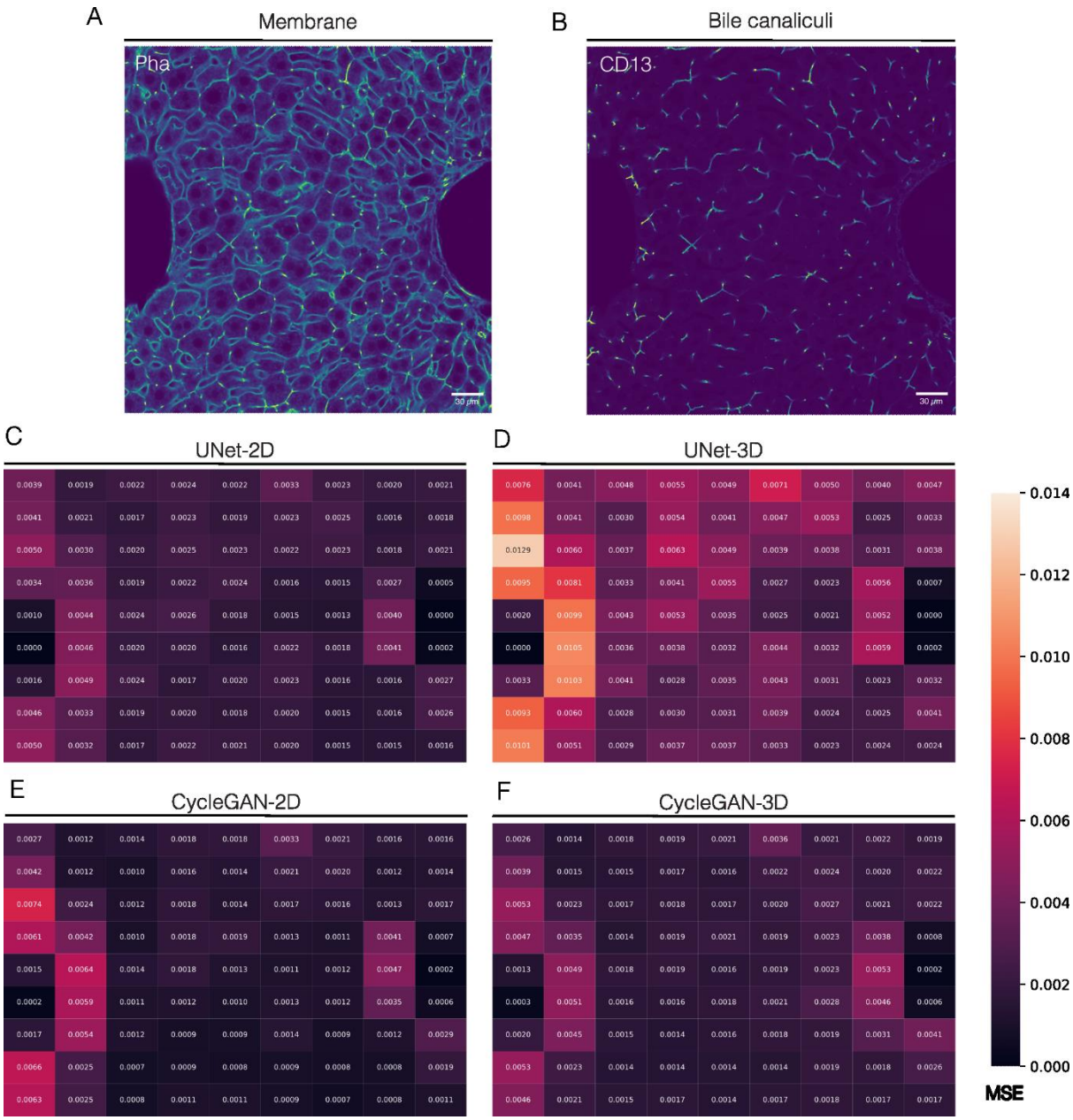

Supp Fig. 2: Artificial neural networks show errors close to veins in mouse tissue. (a-b) Representative images actin mesh (membranes), Bile Canaliculi. (c-f) the images were divided into 9x9 blocks and the mean squared error of the predictions of the different models was calculated and shown as a heat map.

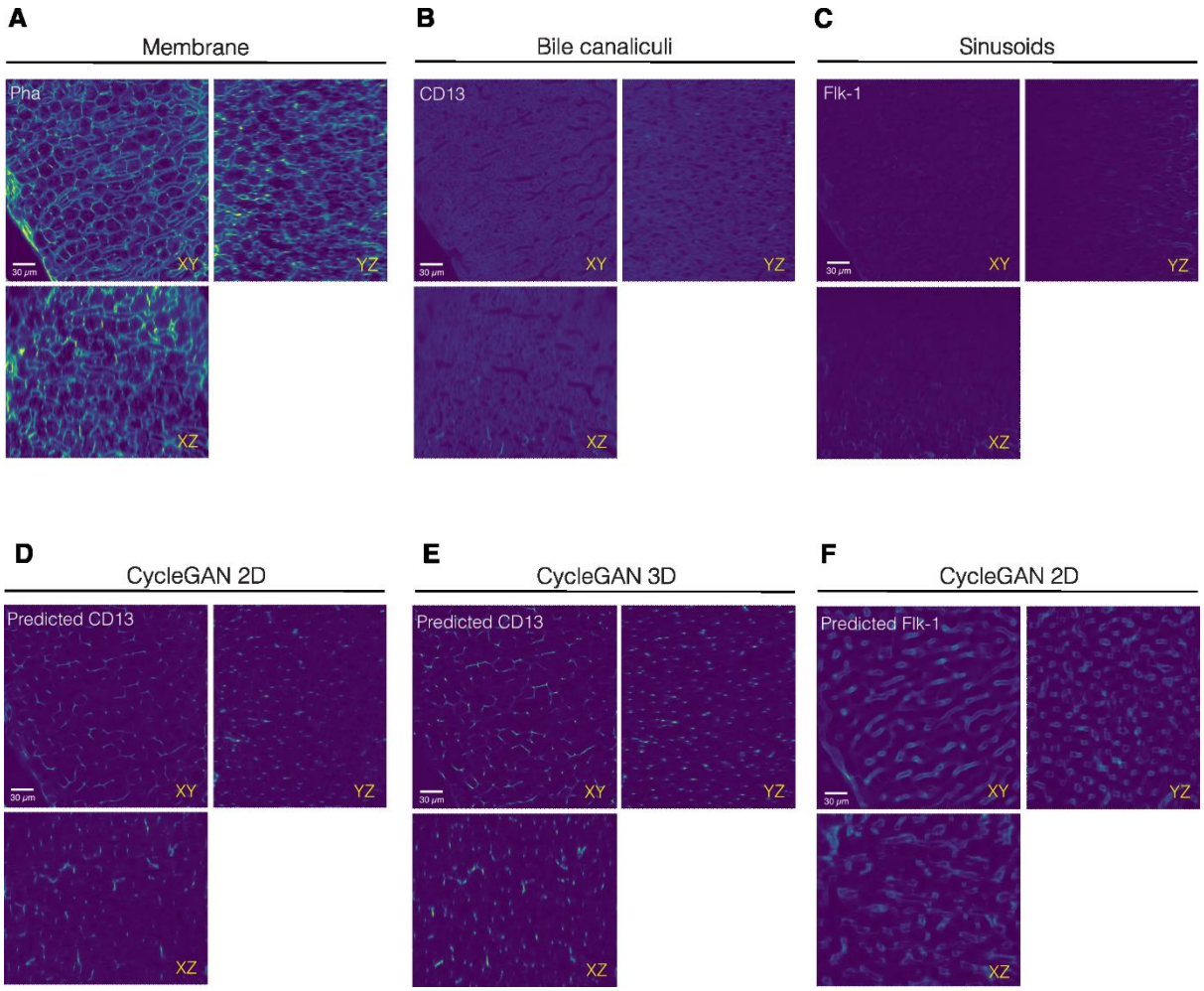

Supp Fig. 3:CycleGAN can predict tissue structures for deep tissue reconstructions. Representative images actin mesh (a), Bile Canaliculi (b) and Sinusoids (c) of mouse liver deep tissue imaging (~200 um) of mouse liver tissue. (c-f) Predictions the BC for 2D and 3D models and Sinusoids for the 2D CyCleGAN model.